

The Open University's repository of research publications
and other research outputs

Analysis of Lunar Boulder Tracks: Implications for Trafficability of Pyroclastic Deposits

Journal Item

How to cite:

Bickel, V. T.; Honniball, C. I.; Martinez, S. N.; Rogaski, A.; Sargeant, H.M.; Bell, S. K.; Czapinski, E. C.; Farrant, B. E.; Harrington, E. M.; Tolometti, G. D. and Kring, D. A. (2019). Analysis of Lunar Boulder Tracks: Implications for Trafficability of Pyroclastic Deposits. *Journal of Geophysical Research: Planets*, 124(5) pp. 1296–1314.

For guidance on citations see [FAQs](#).

© 2019 American Geophysical Union




Version: Version of Record

Link(s) to article on publisher's website:

<http://dx.doi.org/doi:10.1029/2018JE005876>

Copyright and Moral Rights for the articles on this site are retained by the individual authors and/or other copyright owners. For more information on Open Research Online's [data policy](#) on reuse of materials please consult the policies page.

Analysis of Lunar Boulder Tracks: Implications for Trafficability of Pyroclastic Deposits

V. T. Bickel^{1,2} , C. I. Honniball³, S. N. Martinez⁴, A. Rogaski⁵, H. M. Sargeant⁶, S. K. Bell⁷, E. C. Czaplinski⁸ , B. E. Farrant⁷, E. M. Harrington⁹ , G. D. Tolometti⁹, and D. A. Kring^{10,11}

¹Department Planets & Comets, Max Planck Institute for Solar System Research, Göttingen, Germany, ²Department of Earth Sciences, Swiss Federal Institute of Technology, Zurich, Switzerland, ³Department of Earth and Planetary Science, University of Hawai'i, Honolulu, HI, USA, ⁴Department of Earth and Environmental Sciences, Tulane University, New Orleans, LA, USA, ⁵Department of Geology and Geological Engineering, South Dakota School of Mines and Technology, Rapid City, SD, USA, ⁶School of Physical Sciences, The Open University, Milton Keynes, UK, ⁷School of Earth and Environmental Science, University of Manchester, Manchester, UK, ⁸Arkansas Center for Space and Planetary Sciences, University of Arkansas, Fayetteville, AR, USA, ⁹Department of Earth Sciences, University of Western Ontario, London, Ontario, Canada, ¹⁰Universities Space Research Association, Lunar and Planetary Institute, Columbia, MD, USA, ¹¹NASA Solar System Exploration Research Virtual Institute, Mountain View, CA, USA

Key Points:

- Bearing capacity of pyroclastic, mare, and highland regions is calculated based on measurements of boulder tracks in orbital images
- Results agree with calculations based on in situ data—pyroclastic areas show no evidence of lower trafficability than maria and highlands
- Sinkage of proposed mobility systems is estimated, which can be applied to rover requirements, traverse planning, and civil engineering

Supporting Information:

- Supporting Information S1

Correspondence to:

V. T. Bickel,
bickel@mps.mpg.de

Citation:

Bickel, V. T., Honniball, C. I., Martinez, S. N., Rogaski, A., Sargeant, H. M., Bell, S. K., et al. (2019). Analysis of lunar boulder tracks: Implications for trafficability of pyroclastic deposits. *Journal of Geophysical Research: Planets*, 124. <https://doi.org/10.1029/2018JE005876>

Received 6 NOV 2018

Accepted 9 APR 2019

Accepted article online 16 APR 2019

Abstract In a new era of lunar exploration, pyroclastic deposits have been identified as valuable targets for resource utilization and scientific inquiry. Little is understood about the geomechanical properties and the trafficability of the surface material in these areas, which is essential for successful mission planning and execution. Past incidents with rovers highlight the importance of reliable information about surface properties for future, particularly robotic, lunar mission concepts. Characteristics of 149 boulder tracks are measured in Lunar Reconnaissance Orbiter Narrow Angle Camera images and used to derive the bearing capacity of pyroclastic deposits and, for comparison, mare and highland regions from the surface down to ~5-m depth, as a measure of trafficability. Results are compared and complemented with bearing capacity values calculated from physical property data collected in situ during Apollo, Surveyor, and Lunokhod missions. Qualitative observations of tracks show no region-dependent differences, further suggesting similar geomechanical properties in the regions. Generally, bearing capacity increases with depth and decreases with higher slope gradients, independent of the type of region. At depths of 0.19 to 5 m, pyroclastic materials have bearing capacities equal or higher than those of mare and highland material and, thus, may be equally trafficable at surface level. Calculated bearing capacities based on orbital observations are consistent with values derived using in situ data. Bearing capacity values are used to estimate wheel sinkage of rover concepts in pyroclastic deposits. This study's findings can be used in the context of traverse planning, rover design, and in situ extraction of lunar resources.

Plain Language Summary Future explorers will be visiting pyroclastic deposits for research and resource extraction. However, the properties of the surface are not well known and it is unclear how well vehicles and humans are able to travel across these areas. Properties of 149 boulder tracks are measured in spacecraft imagery and are used to derive estimations for the strength of pyroclastic, mare, and highland area material from the surface down to ~5-m depth. Results are compared and complemented with soil strength estimates that have been derived based on in situ measurements taken during previous lunar surface missions. In all regions of interest, tracks have similar appearances, implying that the surface material has comparable properties. Generally, soil strength increases with increasing depth and decreases with higher local slope angles. At depth, pyroclastic deposits show equal or significantly higher strength in comparison to mare and highland areas and, therefore, might be equally trafficable at surface level. Calculations based on globally distributed spacecraft images agree with values derived from Apollo-era in situ data. Based on the soil strength, the sinkage of rovers in the areas of interest is estimated. Potential applications of this work include rover design and mission planning, infrastructure construction, and resource extraction.

1. Introduction

As a new era of lunar exploration begins, attention has turned to lunar pyroclastic deposits (LPDs) as high-priority targets for scientific research and in situ resource utilization (ISRU). These unique locations may be

important sources of volatiles such as OH and/or H₂O (referred to in this work as water) that can be utilized for long-term human exploration. A pyroclastic vent in the Schrödinger basin may be, for example, the largest indigenous source of water in the south polar region (Kring et al., 2014). In addition to being a source of water, the surfaces of glassy material in these types of deposits can be enriched by factors of 3 to 400 in Ag, Br, Cd, Cu, S, and Zn relative to their interiors (Baedeker et al., 1974; Chou et al., 1975; Wasson et al., 1976). Modest chemical etching or abrasion may remove the elements for ISRU. More importantly, pyroclastic deposits with significant FeO and/or the mineral ilmenite can be reduced to produce oxygen needed for consumption by crew and as propellant (Allen et al., 1996). The pyroclastic material is also a suitable building material. Aside from the economic potential of LPDs, they provide a wealth of geologic information about the thermal and magmatic evolution of the Moon, as specified in a report of the National Research Council about The Scientific Context for Exploration of the Moon (National Research Council (NRC), 2007). Pyroclastic deposits can be used to determine the origin and variability of lunar basalts, determine the compositional range of LPDs, and determine the flux of lunar volcanism and its evolution through space and time. In general, pyroclastic deposits provide a window into the lunar mantle, the magmas generated there, and the igneous evolution of the Moon.

Several newly proposed landing sites and traverses exist in the proximity of LPDs (Allender et al., 2019; Kring & Durda, 2012; Potts et al., 2015; Steenstra et al., 2016). In particular, an immense ~400-m-tall pyroclastic deposit in the Schrödinger basin on the lunar farside was among the Tiers I and II targets during the Exploration Systems Mission Directorate phase of the Lunar Reconnaissance Orbiter (LRO) mission because of its ISRU potential for future human missions. Thus far, three landing site and traverse studies have explored the feasibility of crew working in the vicinity of that pyroclastic vent (Allender et al., 2019; Bunte et al., 2011; O'Sullivan et al., 2011). Moreover, several human-assisted robotic sample return missions to the same pyroclastic vent have also been explored (Potts et al., 2015; Steenstra et al., 2016). In all cases, it was assumed trafficability would be possible along the periphery of the deposit, but it remains uncertain if a rover can operate in proximity of the vent center. To further assess missions to the pyroclastic deposit in the Schrödinger basin and LPDs elsewhere on the Moon, additional information about the geomechanical properties is needed to optimize rover design and reduce operational risk of trafficability.

Lunar exploration has historically been plagued with uncertain assessments of trafficability. Despite a first successful soft landing of the Soviet Union's Luna 9 probe in 1966, concerns remained that the lunar surface would not be traversable; that is, the regolith would not be able to bear any kind of load (Carrier et al., 1991). Those concerns were addressed by several NASA Surveyor missions that provided opportunities to analyze the mechanical properties of the lunar regolith in situ (National Space Science Data Center, 2006). In addition, NASA's Lunar Orbiter missions from 1966 to 1967 (LPI USRA, n.d.) returned photographs of the surface, which led to the discovery of boulder tracks carved by rockfalls. These boulder tracks were studied (Eggleston et al., 1968; Filice, 1967; Hovland & Mitchell, 1971 & 1973; Moore, 1970; Moore et al., 1972; Pike, 1971) to derive geomechanical properties of the lunar regolith in regions not been directly sampled by landers. Results suggested crew and rovers would be able to traverse the surface safely.

Mobility was first demonstrated in 1969 by astronauts Armstrong and Aldrin walking over distances of ~100-m around the Apollo 11 landing site (NASA Apollo 11, 2017). The use of rovers began in 1970 with the Soviet Union's Lunokhod 1 (Carrier et al., 1991; IEEE Spectrum, 2010). This rover was followed by the Modular Equipment Transporter (MET) (1971), the Lunar Roving Vehicle (LRV) (1971–1972), the Union of Soviet Socialist Republic's USSR's Lunokhod 2 rover (1973), and the Chinese Yutu rover (2013, Carrier et al., 1991; National Space Science Data Center, 2016, 2017; ESA EO, n.d.-a). On 3 January 2019, the Chinese Chang'e-4 probe delivered a second Yutu rover to the lunar surface that is currently exploring a part of the South Pole-Aitken basin on the farside of the Moon (ESA EO, n.d.-b). In addition, the Indian Space Research Organization is planning to deploy a rover as part of the upcoming Chandrayaan-2 mission, in early 2019 (ISRO, n.d.). The tracks created by astronauts, rovers, and landers provided additional information about the geomechanical properties and trafficability of the lunar regolith (Costes et al., 1970; Mitchell, Carrier, et al., 1972; Mitchell et al., 1974; Scott et al., 1971; Slyuta, 2014). Despite a general level of success, operational limitations were also noted. During its first use around the Apollo 15 landing site, the LRV entered an area of soft soil and experienced 100% wheel slip (Costes et al., 1972). To resolve the issue, the astronauts manually moved the vehicle out of the trench to continue the traverse (Carrier et al., 1991; Costes et al., 1972). Lunokhod 2 encountered soft soils on the inside walls of craters and at the base

of slopes. While its wheel sinkage was normally 2 cm, it increased to >20 cm near some impact craters (Carrier et al., 1991; Florensky et al., 1978). Incidences such as these are of concern when planning robotic missions that will not be able to be corrected manually.

The previous missions occurred in highland and mare terrains. LPDs have only been traversed along their periphery (e.g., Apollo 17), and availability of in situ data for them is limited. Thus, if they are to be explored successfully in the future, a geomechanical assessment must be performed. Recent spacecraft missions, such as NASA's LRO, have produced high-resolution imagery of boulder tracks that are suitable for that assessment. Here those boulder tracks are used to determine the ultimate bearing capacity of LPDs from the near surface to a depth of ~5 m and compared with similar analyses of lunar highland and mare regions.

Ultimate bearing capacity is one measure of the trafficability of a surface material, which is a term that describes the ability of a soil to bear a load, to provide sufficient traction for propulsion, and other locomotion-related properties (Bekker, 1956; Carrier et al., 1991). The derived bearing capacity has been used to estimate the sinkage of current and future rover concepts in the investigated regions. In addition, we explore how bearing capacity can be used to adjust important rover specifications such as total allowable vehicle mass as a function of wheel or footpad dimensions. The results of this work can be used to reduce the risk of robotic and human traverses, while also providing a baseline needed to design infrastructure used for ISRU and large scientific instrumentation such as telescopes.

The available data and the selection of LPDs for this study are described in section 2, followed by a mathematical description of bearing capacity theory. Section 3 describes the measurements made in high-resolution orbital images. Section 4 presents and discusses the results. Finally, in section 5, the implications of those results are provided along with an outlook for application in future missions.

2. Methodology

This work compares the ultimate bearing capacity of lunar regolith in LPDs, mare, and highland regions as a potential measure for their trafficability. Using the Terzaghi (1951) bearing capacity equation (used during the Apollo era for site assessments; e.g., Moore, 1970) and Hansen's (1970) updated equation for shallow foundations, bearing capacity is calculated using values derived from measurements of boulder tracks. Orbital imagery is used to identify and measure these boulders and their associated tracks. In addition, track appearances and shapes in all regions of interest are compared in a qualitative manner as an additional measure for regolith behavior and strength. Soil mechanical values used in the two equations are retrieved from literature pertaining to the Apollo soils. Data measured in photographs taken during the Apollo and Surveyor missions, as well as data measured in situ during the Lunokhod missions, are used to derive bearing capacity values for comparison with the remotely measured data.

2.1. Site Selection and Orbital Imagery

High-resolution orbital imagery allows for the assessment of trafficability in LPDs by measurements of boulder tracks from rockfalls. LPDs range in size from less than 1,000 to 49,013 km² or more (Gaddis et al., 2003). This study focused on large deposits (i.e., those with 600 km² or more) that contain rockfalls with boulder tracks. Large deposits have been chosen, because they provide the most opportunity for selection of potential landing and traverse sites. A total of eight LPDs are investigated (Table S1 in the supporting information, generally denoted S). Additionally, the selected LPDs have been evaluated for their TiO₂ and FeO content, plus theoretical and experimental water content (Table S1). Figure S1 displays the locations of all boulder tracks used for this study.

In order to achieve sufficient measurement accuracy, image data with the highest possible spatial resolution and quality are required. Seventy-nine LRO Narrow Angle Camera (NAC) images that contain boulder tracks have been processed from experimental data record level 0 to reduced data record level 2, with spatial resolution ranging from 0.38 to 1.68 m/pixel. Subsequently, all images have been adjusted to the appropriate projection in ArcGIS 10.1 using Isis3. The LRO Wide Angle Camera (WAC) DTM GLD 2013 100 m (Scholten et al., 2012) was used for measurements relating to slope and elevation. See Figure S2 for a detailed image processing workflow.

2.2. Bearing Capacity Equations and Calculations

Analysis of boulder tracks on the surface of the Moon has been used to estimate the bearing capacity of regolith since the Lunar Orbiter program began imaging the lunar surface in 1966 (Eggleston et al., 1968; Filice, 1967; Moore, 1970). The ultimate bearing capacity is the maximum load the ground can sustain before failure (Meyerhof, 1951). It is a potential measure for a soil's trafficability, a term that not only describes the ability of a soil to bear a load (i.e., the sinkage of a load into the surface) but also whether a soil is able to provide traction as well as propulsion (Bekker, 1956; Carrier et al., 1991). Other aspects of trafficability describe terrain, energy consumption of a vehicle due to surface roughness, and rolling resistance (Bekker, 1956; Carrier et al., 1991). Because ultimate bearing capacity denotes the at-failure state of the soil, the driving forces (boulder weight) and the resisting forces (shear strength of the soil) are equal and cancel out. This means that the weight of the boulders can be neglected (i.e., no density measurements of the boulders are required) while only intrinsic soil properties are used.

Amongst the available bearing capacity equations, Terzaghi (1951), equation (1)) has traditionally and widely been used by geotechnical engineers. In addition, Hansen (1970), equation (6)) incorporates various adaptations and expansions to Terzaghi's approach, to better address the contact interface between an imposing object (whether it be a boulder or mechanical system) and a geologic surface. For these reasons, both approaches are explored in this work.

2.2.1. Terzaghi

Terzaghi's (1951) ultimate bearing capacity (q_f) formula for shallow circular footings (equation (1)) consists of three terms that represent the total shear strength of the soil, that is, the cohesion, the soil surcharge, and the soil friction along the footing:

$$q_f = 1.3cN_c + q_0N_q + 0.3\gamma_s B_{av}N_\gamma \quad (1)$$

where c is the cohesion of the soil, q_0 is the vertical stress within the soil, and γ_s is the unit weight of a homogeneous isotropic soil. B_{av} is the diameter of the circular footing, which is the average of the two effective horizontal footing dimensions B_T and L_T as derived using Figure S3. The surcharge q_0 is the product of the depth of track (i.e., depth of footing, D) and the soil unit weight (γ_s), which is derived from the density of soil (ρ) and gravity on the Moon (g_M). Depth of track is calculated using the shadow length (S) that is cast within the track and the incidence angle (i) of the Sun:

$$D = S / \tan(i) \quad (2)$$

Lastly, the bearing capacity factors (N_c , N_q , N_γ) are derived from Terzaghi (1951), equations (3) and (4)) and Coduto et al. (2011), equation (5)):

$$N_q = \frac{e^{(\frac{3\pi}{4} - \frac{\phi}{2}) \tan(\phi)}}{2 \cos^2(45^\circ + \frac{\phi}{2})} \quad (3)$$

$$N_c = (N_q - 1) - \cot(\phi) \quad (4)$$

$$N_\gamma = \frac{2(N_q + 1) \tan(\phi)}{1 + 0.4 \sin(4\phi)} \quad (5)$$

where ϕ is the internal friction angle, which is the angle between the shear stress and the normal effective stress where shear failure in a dry granular material occurs (e.g., Melosh, 2011).

Terzaghi's equation assumes that lunar boulders are spheroids and, thus, have a circular footprint. A circular footing is not entirely representative of the observed shapes of lunar boulders and the pressure acting onto the surface through a sphere but has been used in the past and is used as one possible approximation for this study because a realistic reproduction of the exact boulder surfaces is beyond the scope of this work. Terzaghi's bearing capacity equation (equation (1)) also assumes that the base of the footing is rough and requires that the depth of track is less than the width of footing, that is, either the respective boulder diameter or the track width, depending on the observed displacement method (Figure S3). In general, Terzaghi's equation does not consider inclined terrain and, thus, overestimates the bearing capacity for sites located on slopes (Castelli & Lentini, 2012; Meyerhof, 1957).

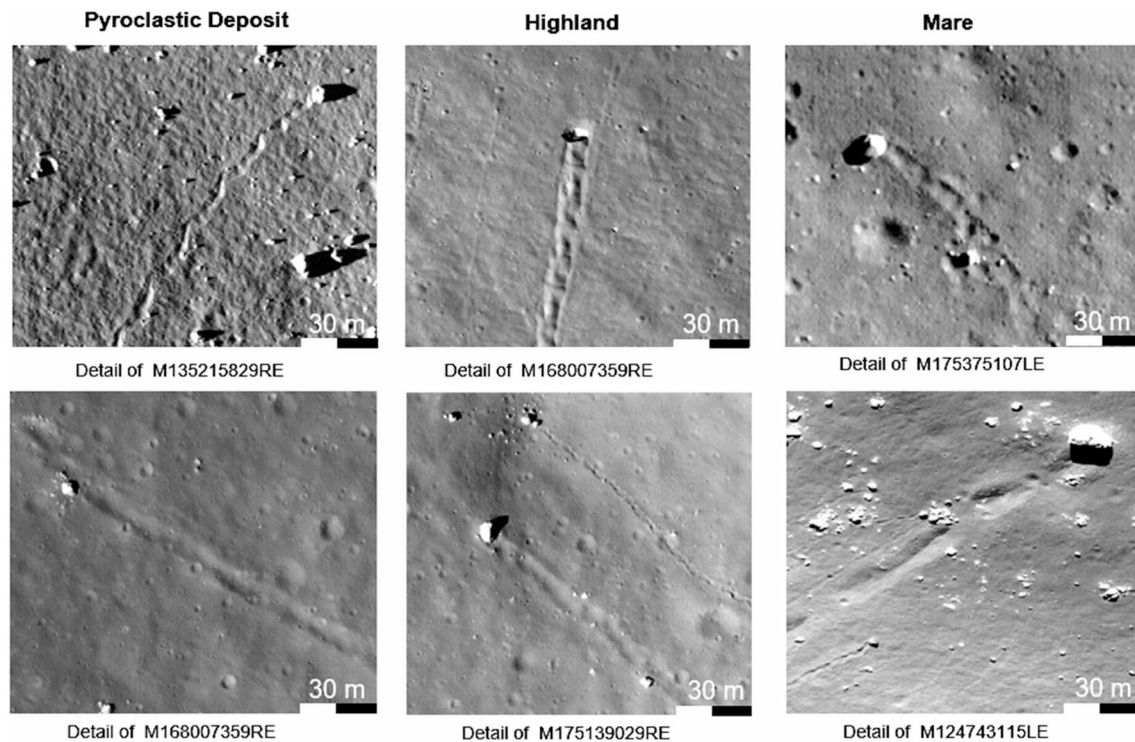


Figure 1. Qualitative comparison of boulder track shape and appearance in mare, highland, and LPDs; no differences in appearance suggest similar geomechanical properties of material. Tracks with potential inertial soil responses and rounded edges are displayed in the second row. North is up. LPDs = lunar pyroclastic deposits.

Boulder tracks produced at the source of the track and at the terminus are measured. At these locations, it is assumed that the boulder has minimal kinetic energy and can be approximated as a static load. While the soil reacts with inertial resistance upon dynamic impacts, the assumption of a static load will result in conservative bearing capacity values (Carrier et al., 1991; Hovland & Mitchell, 1973; Moore et al., 1972). The static assumption is also useful to generalize the otherwise complex lunar boulder displacement methods that have been observed, that is, jumping, rolling, sliding, and their influence on bearing capacity (Figure 1).

2.2.2. Hansen

It has been shown (Shill & Hoque, 2015) that bearing capacity estimations using Terzaghi's formula tend to deviate from results using other equations, particularly at higher friction angles. In addition, Terzaghi's approach does not consider a number of variables such as the local slope. For those reasons, an additional approach is considered in this work. Hansen's (1970) equation for shallow foundations (equation (6)) utilizes a different weighting to the bearing capacity factors (equations (7)–(9)) and considers depth factor $d_{(c,q,\gamma)}$ (equations 2.2.2–5*–2.2.2–13*), shape factor $s_{(c,q,\gamma)}$ (equations 2.2.2–14*–2.2.2–16*), and local slope inclination factor $g_{(c,q,\gamma)}$ (equations 2.2.2–17*–2.2.2–18*; * in the supporting information). The formula also considers load inclination $i_{(c,q,\gamma)}$ and foundation (boulder) inclination $b_{(c,q,\gamma)}$ factors. Hansen's additional factors are valid if (1) the local slope angle is smaller than the material's internal friction angle and (2) the local slope angle plus footing inclination angle is smaller than 90° (Hansen, 1970). As the dynamic displacement component is being neglected and as observations indicate that rockfalls carve into the slope substrate, this study assumes that the curved surface underneath a boulder on a slope can geometrically be described as a horizontal plane at each point x in time and, thus, there is no footing and load inclination to account for. Consequently, all i and b factors have been set to 1. This general assumption is equally valid for boulders of various sizes, including rover wheels and boots, and has been used by previous studies, such as that by Hovland and Mitchell (1971), in a similar manner.

In contrast to the selected equation from Terzaghi for circular foundations, the Hansen formulae approximate rectangular footings and are given by Hansen (1970) and Bowles (1997) as

$$q_f = cN_c s_c d_c i_c b_c g_c + q_0 N_q s_q d_q i_q b_q g_q + 0.5 \gamma B_H N_\gamma s_\gamma d_\gamma i_\gamma b_\gamma g_\gamma \quad (6)$$

$$N_q = e^{\pi \tan \phi} \tan^2 \left(45^\circ + \frac{\phi}{2} \right) \quad (7)$$

$$N_c = (N_q - 1) \cot(\phi) \quad (8)$$

$$N_\gamma = 1.5(N_q - 1) \tan(\phi) \quad (9)$$

The depth and shape factors are dependent on the orientation of the boulder during its displacement, which means that the input parameters for foundation width (B_{Hb} , short boulder diameter) and length (L_{Hb} , long boulder diameter) have to be determined based on observations using the schematic in Figure S3. The measurements can then be applied in equations 2.2.2–5 through 2.2.2–16, listed in the supporting Information. The slope inclination factor can be derived by using equations 2.2.2–17 and 2.2.2–18 in the supporting information.

Other methods and modified approaches to calculate bearing capacity of soils such as Hovland and Mitchell (1971), Vesic (1973), Durgunoglu and Mitchell (1975), Kusakabe et al. (1981), Saran et al. (1989), and Eurocode7 (1996) have been developed. However, besides minor mathematical and methodical differences between Hansen (1970) and these approaches, previous studies such as Shill and Hoque (2015) have shown that most methods produce similar bearing capacity results. Due to that finding and a realization that some of these approaches rely on outdated assumptions due to the data quality at that time, only the bearing capacities calculated with the original Terzaghi (1951), equation (1)) and Hansen (1970), equation (6)) equations will be analyzed and compared in this work, using improved assumptions that are based on new high-resolution image data from LRO.

2.3. Trafficability

The ultimate bearing capacity of regolith can be used as a measure for its trafficability, that is, if the soil is able to support a vehicle or astronaut, which is a fundamentally important question that has to be answered prior to the deployment of human or robotic assets in unknown regions, to avoid loss of mobile assets due to stalling. A load will cause the regolith to fail in shear until a layer that is able to bear it is reached and is therefore an indirect measure for the sinkage of a load into the soil, for example, a rover wheel or a robot's footpad, also referred to as flotation. Since failure and therefore sinkage stops as soon as load pressure and bearing capacity are equal, the basic relation

$$q_f = \frac{mg_M}{A_{\text{eff}}} \quad (10)$$

can be used to estimate sinkage, with m as the mass of the object under consideration and A_{eff} as the effective area of contact with the surface. For lander footings, rover legs with plane footpads, or astronaut boots, the effective area A_{eff} will be always equal, regardless of the sinkage into the soil. For round rover wheels however, the effective contact area will increase as the wheel begins to sink into the soil, until the point where it has sunk into the soil up to its center, that is, its radius. The same is valid for curved footpads of leg-wheel rover hybrids, such as RHex- and SpaceBok-type rovers (Boston Dynamics, 2019; SpaceBok, 2017, Figures S4 and S5); however, the calculation of their contact area is slightly more complex. Bekker (1956, 1960) stresses that usage of soil shear strength as a measure for trafficability is precarious and always dependent on the shape of the wheel/pad-ground contact area. Therefore, Bekker (1960) recommends to conduct shear strength-based sinkage estimations only for vehicles with strip-like contact areas, that is, with wheel/pad width to diameter ratios of less than ~ 0.5 (class II or higher). This criterion is being met by all assessed wheeled rover and all hybrid rover designs (Table S2). For this work, the footpads of legged rovers, such as Spot-type robots (Boston Dynamics, 2019), have been approximated as wheels, due to their shape.

In this study, equation (10) is used to provide an estimate of sinkage using ultimate bearing capacity but does not consider soil compaction, dilatancy, or effects caused by elastic wheel deformation and across-profile wheel or footpad curvature. In addition, the sinkage is estimated assuming a static load scenario, that is, no movement of the rovers is considered. The estimations based on equation (10) also assume that the

wheel or pad has a closed and solid surface. This study estimated wheel or leg sinkage of current and future wheel-based rover designs such as the Lunar Electric Rover (LER, also known as Space Exploration Vehicle), Resource Prospector, and Yutu (Figures S5a–S5c), as well as of leg-based or hybrid robots such as SpaceBok-, Spot-, and RHex-type rovers (Figures S5d–S5f).

2.4. Soil Mechanical Properties

Lunar soil mechanical properties such as density, cohesion, and internal friction angle have been estimated throughout literature, often resulting in a wide range of results (Carrier et al., 1991). Therefore, a range of values have been used when calculating bearing capacity of the lunar surface and the associated friction angle, making the results difficult to compare (Hovland & Mitchell, 1969; Hovland & Mitchell, 1973; Moore, 1970). Generally, the soil property values used in the literature represent bulk lunar soil. In order to calculate bearing capacities at different locations on the lunar surface, specific soil property values have been obtained for each LPD, highland, and mare regions. Soil density values have been selected from Apollo core tube analyses that best represent LPD, highland, and mare material (Table S3). For each location, density values for the top 30 cm and lower than 30 cm of regolith are available. The top 30 cm represents the soil that will be considered for calculations in the shallow depth domain (rover tracks and shallow boulder tracks), while the density below 30 cm will be used for calculations of boulder tracks that run deeper than the indicated shallow domain. Cohesion values have been calculated in previous studies based on measurements taken on the lunar surface and produce a range of values of 0.1 to 4.9 kN/m² (Carrier et al., 1991). Boreholes drilled during the Apollo 16 and 17 missions remained open after the drill stem has been withdrawn, demonstrating the significant cohesion of the lunar regolith (Carrier et al., 1991). For the bearing capacity calculations in this work, an estimate of 1 kN/m² is used for cohesion (Hovland & Mitchell, 1971; Mitchell, Houston, et al., 1972).

The angle of internal friction is dependent on the local context and conditions of the soil, including porosity, density of stratification, and the shape of particles (e.g., sphericity, smoothness, and roundness; Melosh, 2011; Cho et al., 2007). Authors such as Melosh (2011), Mitchell, Houston, et al. (1972), and Mitchell et al. (1974) provide values ranging from around 13 to 50° for lunar soils and terrestrial analogs, based on in situ and remote measurements. Despite this wide range, the use of isolated friction angle parameters out of their original spatial context might add uncertainties to the bearing capacity calculations, particularly as this parameter is decisive for the accuracy of the calculations (the *N* factors in particular). In lieu of the absence of site specific literature values, the angle of repose of shallow granular flows is measured in six high-resolution NAC-based digital elevation models (DEMs). The DEMs have been processed for mare, highland, and LPDs using the Ames Stereo Pipeline (Shean et al., 2016, details about the DEMs are displayed in Table S4). The internal friction angle of a dry granular mass expresses itself as the so-called angle of repose, that is, the maximum angle at which a loose pile of material still stands stable (Melosh, 2011). By measuring the local slope angle of flow features at their toe, the internal friction angle can be closely approximated, assuming that the material of the flow is the same as the substrate. The respective measurements are performed across several shallow granular flow-like features to derive a representative average. The resulting friction angle values are 28° for mare material, 30° for highland material, and 31° for LPD material, which is a significant refinement of literature values.

3. Measurements

A total of 149 boulder tracks are used to make eight unique measurements for the bearing capacity calculations. Measurements include long (*L*) and short diameters (*B*) of the boulder, track width (*W*), shadow length within the boulder track (*S*), and local slope (β), according to Figures S3 and S4. All measurements are taken near the boulder's terminus and near its origin (static assumption). The width and shadow length measurements are conducted 3 times for each of the individual tracks whenever possible. One source of variability in boulder track measurements results from irregular tracks where the track width changes due to wobbling along the track. Such effects have been minimized through average measurements where data were obtained at maximum, minimum, and intermediate width. Further, tracks that show signs of a strong inertial response, such as rounded edges, have been measured in a conservative way, that is, using the distance between the inner rim of the two exterior track bulges.

Measurements of shadow length are performed on the same segment of track as the corresponding width measurements. Track shadow length near the boulder as well as the source are both measured by determining the location of the Sun and then measuring shadow length parallel to direction of illumination. Images in which the shadow length is perpendicular to the track provide the most accurate measurements. Inaccuracies occur when the shadow is not perpendicular to the track, in which case a shadow length measurement should be taken parallel to the Sun direction (Figure S6). This should result in an equivalent shadow length measurement if the boulder track has spherical track elements. However, if the boulder track does not contain spherical boulder footprints and the Sun orientation is not parallel to the track, then a potentially misleading shadow length will be measured. Data that do not meet the criteria for a correct shadow length will not be considered in this work. As the derivable track depth depends on the measurable shadow length (equation (2)), the spatial resolution of LRO's NAC of ~ 0.5 m/pixel is limiting the ability of the technique to calculate bearing capacities at very shallow depths, that is, between surface level and ~ 0.35 m. However, using imagery with very high solar incidence angles that cause long shadows even for very shallow tracks, the available horizontal resolution is sufficient to sample shadow length and, thus, track depth as small as ~ 0.19 m.

Slope for the boulder and source locations is determined from the 100-m resolution, global LRO WAC stereo-derived DEM (Scholten et al., 2012). As the spatial resolution of this DEM is coarse in comparison to the size of boulders, three high-resolution DEMs (2 to 10 m/pixel) for highland, mare, and LPD sites have been produced with the Ames Stereo Pipeline (Shean et al., 2016, details about the DEMs are displayed in Table S4). These NAC DEMs are compared to the global DEM of Scholten et al. (2012) to assess potential uncertainties, which could have been introduced by the use of the lower spatial resolution DEM. The direct comparison suggests that the lower spatial resolution of the used WAC DEM is sufficient and does not influence the accuracy of the slope measurements. All measured data are presented with histograms in Figure S7 with respect to their respective region on the Moon.

In addition to boulder tracks, this study uses measurements performed in photographs taken during the Apollo and Surveyor missions, as well as in situ during the Lunokhod missions. Besides astronauts and rovers (LRV, Lunokhod), the MET and the boulder tracks measured on the ground during Apollo 17 are used for this analysis. The use of in situ data allows for a comparison of the remote sensing-based results and for a calculation of bearing capacity results for shallow depths.

4. Results

Differences in the shape of boulder tracks in mare, highland, and LPDs may indicate differences in geomechanical properties. However, no differences of that type are observed among the regions, implying LPDs have similar geomechanical properties as those in mare and highland regions. Difference in track appearances appears to be influenced instead by boulder shape and displacement method, that is, rolling, sliding, or bouncing, than by region. Figure 1 displays a comparison between boulder tracks in all areas of interest.

In this work, bearing capacity is investigated as a function of depth, slope, and equation used. In addition, the results have been classified by the region and the geomorphological context at which their corresponding measurements have been made. This allows for the comparison of pyroclastic soils with mare and highland material, as well as for the comparison of material on regular slopes, crater slopes, rilles, and pyroclastic vents.

In order to evaluate the deviation in results between the Hansen and Terzaghi equations, the bearing capacity values calculated for all boulders are compared (Figure S8). Both equations provide similar results for lower bearing capacity values. As bearing capacity values begin to increase the correlation between Terzaghi and Hansen weakens. Further, there is a trend in which the Terzaghi method provides generally higher bearing capacity values than Hansen. For both approaches, the N factors are decisive for the calculation of the bearing capacity. To put them into perspective and context, the derived factors for N_c , N_q , N_γ have been plotted in Figure S9. The difference in the N factors is one reason why Hansen produces lower bearing capacity values. Lower values are also a result of the application of correction factors for Hansen (equations 2.2.2-5 through 2.2.2-18) that reduces the bearing capacity, based on the physical conditions and the geometry of the investigated site. As Hansen (1970) partially addresses these uncertainties (e.g., regarding boulder

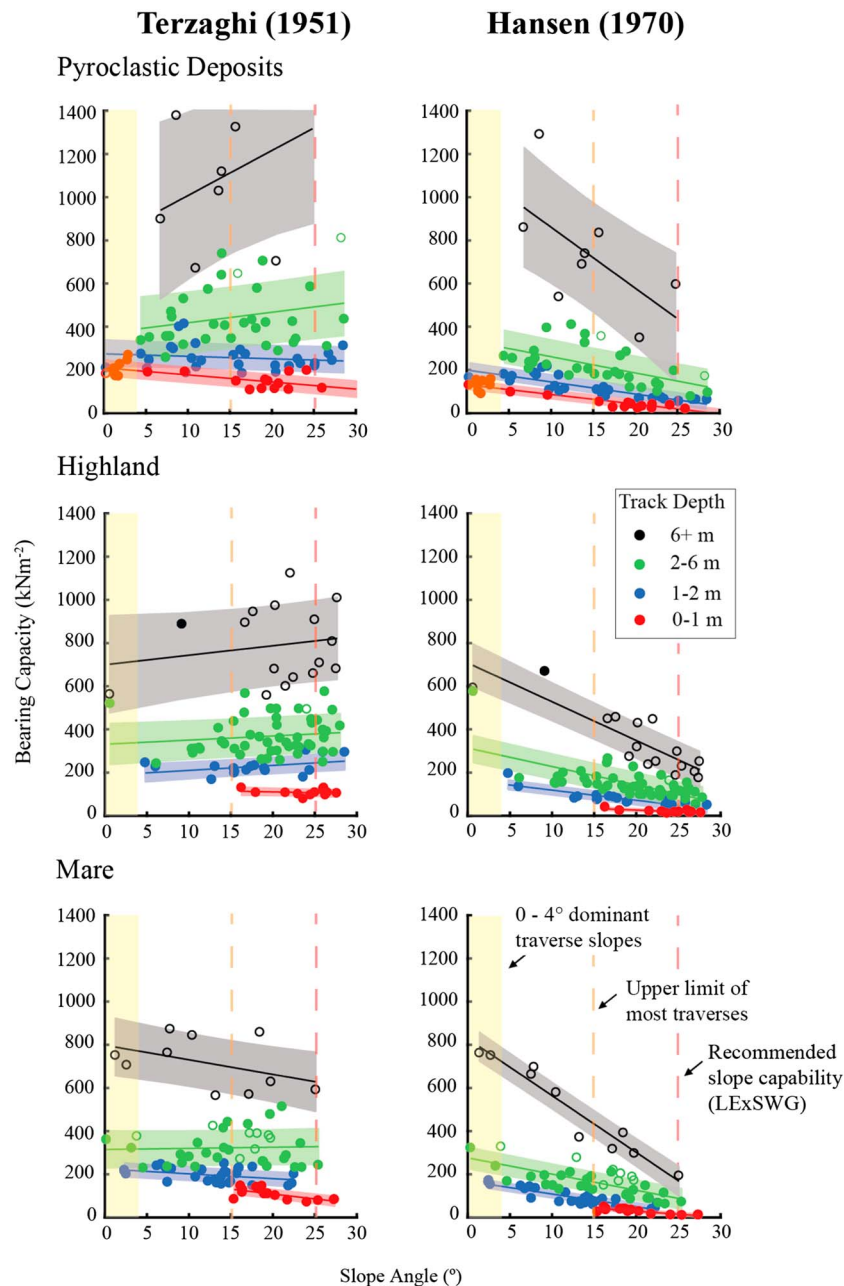


Figure 2. Bearing capacity values are shown here as a function of slope angle. Values are provided from both the Terzaghi and Hansen calculations. Colors correspond to the depth of track from which the values are derived. Hollow circles indicate track depths that exceed local regolith thickness estimates. Slope traverse values are taken from the final report of the Lunar Exploration Science Working Group (LExSWG, 1995).

shape and slope inclination), it is considered the more representative approach for this study, as it provides a better-restricted and realistic lower boundary for the ultimate bearing capacity.

The bearing capacity values at each location type (LPDs, highland, and mare) and in varying geomorphological context are plotted with respect to the local slope angle where the measurements have been taken (Figures 2 and S8). The data are further subdivided by the depth of track. The boulders that are believed to have fully penetrated the surface regolith likely interacted with more consolidated material below. For this reason, these points have been plotted as hollow shapes to indicate that their values may not be

representative of the upper regolith that this study is investigating. The estimate for the local average regolith thickness has been taken from several sources, using the shallowest estimate (see Table S5 and Figure S10). Results are shown for both Terzaghi and Hansen calculated values. A least squares fit has been applied with a shaded error bar derived from an estimate of the standard deviation of the error. As seen in Figures 2 and S8, bearing capacity values increase with increasing depth. The values calculated using Hansen have a greater dependence on slope angle where the bearing capacity decreases with increasing slope angle. Bearing capacity values in mare and highland areas are similar, while LPDs show slightly higher values. An analysis of bearing capacity in relation to slope and geomorphological context shows no significant dependency and, thus, does not indicate a direct potential influence of local context (Figure S11).

Bearing capacity as a function of track depth is presented in Figures 3a and S9 for LPDs, highland, and mare material for both the Terzaghi and Hansen equations. Due to the limitation in spatial resolution of NAC images at around 0.5 m/pixel, no boulders smaller than ~ 1.5 m in diameter can be observed; that is, no shallow boulder tracks can be measured, causing a gap of remote sensing-derived bearing capacity values from 0 to a depth of ~0.19 m in all regions. A least squares fit has been applied, and a shaded error bar derived from an estimate of the standard deviation of the error. Generally, the bearing capacity for each location increases with depth, which is to be expected as the material at depth becomes increasingly compact and less porous (Carrier et al., 1991; Houston et al., 1972; Mitchell, Houston, et al., 1972) and because a larger soil column causes a higher surcharge load (equations (1) and (6)). As in Figures 2 and S6 the Terzaghi equation provides consistently higher estimates for bearing capacity. Hollow data points represent depth measurements that exceed the estimated regolith thickness at the measured location, based on Table S5 and Figure S10. Bearing capacity as a function of depth and geomorphological context does not indicate a significant influence of local context (Figure S12).

To compare the bearing capacity values generated in this work, a two sample *t* test assuming unequal variances (two-tail) was run between each of the three regions for four depth subdivisions (0.19 to 1, 1 to 2, 2 to 6, 6 + *m*), which provided twelve *p* values based on a 95% confidence interval (detailed statistics and results can be found in Table S6). Results indicate that LPDs have equal or significantly higher bearing capacity values for the four investigated depth ranges than mare and highland areas. Mare and highland regions show statistically equal bearing capacities over the entire depth range from 0.19 to 6 + *m*.

Based on the statistical similarity and degree of correlation of bearing capacity over depth between mare and highland regions, the calculated mare and highland bearing capacity values are plotted together and combined with the bearing capacity values calculated using boulder tracks measured in photographs taken during the Apollo 17 mission (Figure 3b). The results from both the in situ and the remotely measured values can be directly compared in the depth range from 0.19 to ~5 m and show a high degree of correlation. Based on this correlation and in order to close the gap between surface level and 0.19-m depth, lines of best fit have been interpolated to link the results based on boulder tracks (remote and in situ) to bearing capacity results calculated with the identical method (Hansen, 1970; Terzaghi, 1951) but using shallower measurements taken from Apollo MET and LRV track photographs in mare and highland regions. These fits consist of three segments in the previously selected depth ranges of 0 to 1, 1 to 2, and 2 to 6 m, cut at 5 m. The derived fit for 0 to 1 m is based on values calculated from the in situ measurements as well as on values derived from boulder track measurements. For the depth range from 1 to 2 and 2 to 6 m only the bearing capacity values calculated based on in situ measurements (Apollo 17 observations of boulder tracks) have been used, because they represent a conservative lower limit for the soils' strength in mare and highland regions at that depth (Figure 3b). The derived equations for the line fits with q_f in kN/m^2 and D in meters are

$$0-1 \text{ m} : \quad q_f = \frac{D + 0.140}{0.026} \quad (11)$$

$$1-2 \text{ and } 2-6 \text{ m} : \quad q_f = \frac{D + 0.596}{0.037} \quad (12)$$

As shown by the statistical analysis, the bearing capacity of LPDs based on boulder tracks appears to be equal or significantly higher than in mare and highland areas along the entire investigated depth range from 0.19

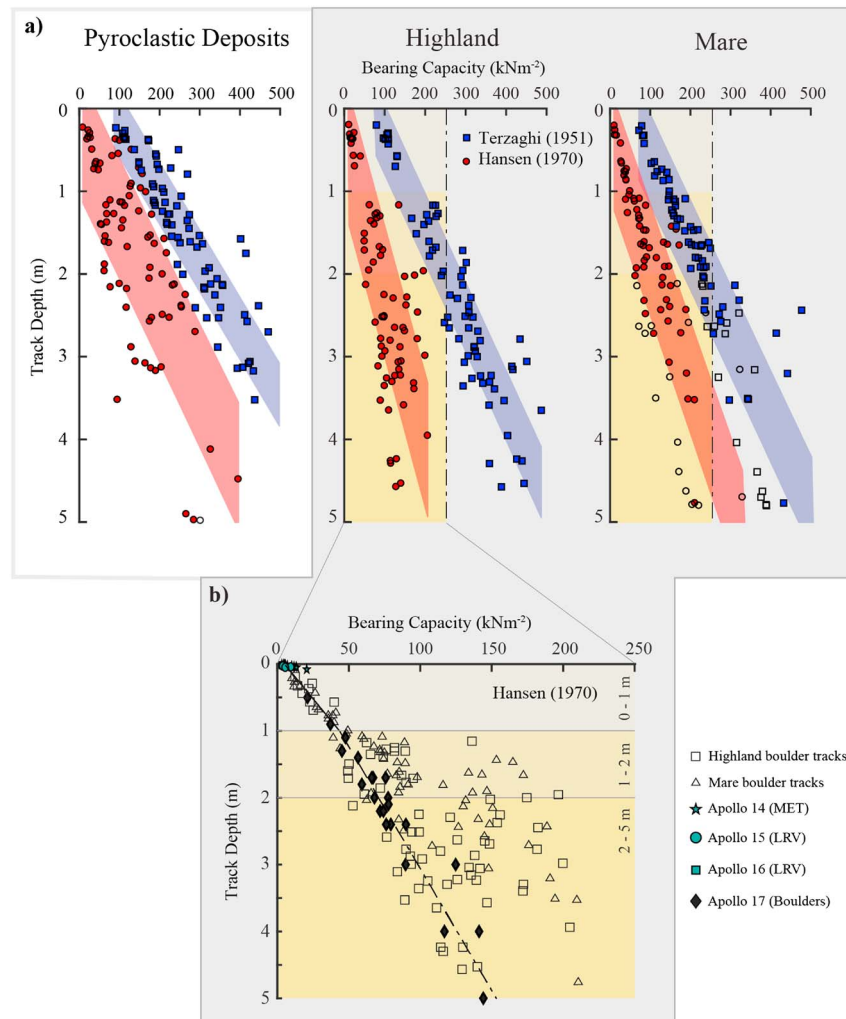


Figure 3. (a) The bearing capacity values for each boulder site are presented as a function of track depth. The vertical line indicates the adapted x axis limit for Figure 3b, while the vertical color gradient indicates depth ranges used in Figure 3b. Hollow shapes indicate boulders that are believed to have cut through the regolith at their location based on estimates taken from sources listed in Table S5/Figure S10. (b) Combination of bearing capacity values (mare and highland) calculated (Hansen, 1970) based on remotely measured data and in situ measured data.

to 5 m. It may, thus, be possible that the derived interpolated linear fit for mare and highland regions represents a conservative lower limit of bearing capacity in LPDs. Based on the assumption that the mechanical behavior of LPDs is only governed by the factors considered by the used equations, the derived lower limit has been extrapolated to close the sampling gap between the surface and 0.19-m depth. This extrapolation is based on the assumption (discussed further below) that soil-strengthening processes such as sintering are absent or do not significantly contribute to the mechanical behavior of LPD regolith in the investigated depth range. The extrapolated linear bearing capacity envelope has been used for the subsequent trafficability analysis. Numerical results of calculated ultimate bearing capacity including associated error for each investigated location type at the specified depth ranges and for varying slope values are displayed in Table S7.

5. Discussion

This study uses observations of tracks carved by rockfalls to derive qualitative and quantitative properties of the regolith in LPDs in comparison to that in mare and highland areas. Hovland and Mitchell (1971) note

that boulder track width appears to be sensitive to changes in regolith conditions. However, observations of boulder track shapes and appearances in the regions of interest did not show any significant differences. Slight differences in track sharpness, clarity, and apparent width equally occur in all investigated regions and could be indicative of an inertial response of the shearing soil that is pronounced due to the lower gravitational acceleration on the Moon, initially caused by very dynamic boulder displacements. Rounded track edges could also express an ongoing erosion over time, for example, driven by microimpacts.

Besides the described Apollo 15 LRV incident, the Soviet Union's Lunokhod 2 rover experienced increased wheel sinkage as it approached the toe of a slope in Le Monnier Crater (Carrier et al., 1991; Florensky et al., 1978). This sinkage indicates a reduction of bearing capacity that could be connected to the geomorphological environment or the genesis of this specific site. Melosh (2011) suggests that slow downslope movement of regolith occurs on lunar slopes, resulting in characteristic slope lobes and textures. Material transport is caused by thermal variations, micrometeorite impacts, seismic shaking, and electrostatic levitation. Downslope movement of regolith implies it accumulates at the bottom of slopes, potentially resulting in an increased regolith thickness and lower bearing capacity values, possibly influenced by a higher porosity of the regolith present (Houston et al., 1972). However, the results derived here do not directly imply reduced bearing capacities at the bottom of slopes. In contrast, soil strength appears to increase with lower slope gradients; that is, it is observed to be higher at the toes of slopes, as it has previously been described by Carrier et al. (1991) based on in situ sampling. On slopes, however, as illustrated by Figures 2 and S9, bearing capacity of lunar regolith generally varies, where higher slope gradients reflect lower bearing capacities. Based on Hansen's (1970) equation, this is caused by the fact that an inclination of the surface results in a reduced soil volume that is bearing the boulder. This reduces the surcharge and friction terms, as well as the bearing capacity (Castelli & Lentini, 2012; Meyerhof, 1957). Results derived with Terzaghi (1951) also show a slight but noticeable decreasing bearing capacity trend with increasing slope angles for very shallow track depths, independent on region or geomorphological context, although the equations do not consider slope inclination (Figures 2 and S8). This could indicate that there is another reason or predisposition that reduces the bearing capacity of lunar regolith on slopes in the depth range from 0 to 1 m, such as potential surficial mass movements as previously suggested by Melosh (2011) or Houston et al. (1972) that form a shallow regolith colluvium with altered mechanical properties.

Cone penetrometer data from human and robotic lunar surface missions indicate a similar behavior of the soil, as regolith has been found to be weaker on slopes than in flat areas, at least down to a depth of 70 cm (Carrier et al., 1991). A direct comparison of different geomorphological settings suggests that bearing capacity of impact crater slopes, regular slopes, slopes in pyroclastic vents, and slopes in rilles is similar over the entire slope angle and depth range (Figures S8 and S9). Therefore, the influence of geomorphology and genesis on regolith bearing capacity in the investigated depth range might be limited or at least less significant than the observed influence of slope angle and location along the slope. However, the technique used in this study to derive bearing capacity has a limited capability to investigate distribution of bearing capacity at very shallow depths ~ 0.19 m and less, due to the limitations in spatial resolution of the used sensor (NAC). Therefore, geomorphology dependent heterogeneities and variations of bearing capacity at shallow centimeter-scale depths on lunar slopes and their toes cannot be ultimately excluded and remain to be tested in situ.

Some clues about the potential properties of pyroclastic material at shallower depths can be gleaned from Apollo 15 and 17 observations of pyroclastic glass deposits. At Apollo 15, where green pyroclastic glass was mixed with other soil constituents, no significant increase in the sinkage of astronauts or the LRV was noted as a function of increasing green color of the soil. At Apollo 17, where a unit of wholly orange and black pyroclastic glass was exposed at the surface, no increase in sinkage was observed (e.g., NASA images A17-137-20986 and A17-137-20990; Muehlberger et al., 1973). Near Shorty Crater, where a deposit of pyroclastic glass is exposed at the surface (0 cm) and extends to a depth of at least 70 cm, the bearing capacity is similar to, if not greater than, that of nearby pyroclastic-poor soils. It is so remarkable that Mitchell et al. (1973) reported the orange pyroclastic soil is *unusually compact and exhibits high cohesion*. The material was affected by the Shorty Crater impact event but that would have had a tendency to reduce cohesion, not increase it. Moreover, no degradation of that cohesion seems to have occurred over the past 19 Myr (Eugster et al., 1977) after being reexposed by the Shorty Crater impact event.

Rover traverse planning draws on extensive use of slope maps to determine whether rovers are able to access specific regions of interest, as wheels tend to be susceptible to slip as slope gradients increase. However, the results of this study imply that trafficability analyses should also consider variations, and potentially heterogeneities, of bearing capacity along slopes to prevent rovers from unfavorable wheel sinkage. In addition, knowledge about variations of wheel sinkage along slopes based on bearing capacity might help optimize rover wheel design to trade-off sinkage and traction for on-slope propulsion.

The observed increase of bearing capacity with increasing depth (Figures 3 and S9) is expected and is caused by the decrease of soil porosity and an increase of the soil surcharge shear strength term that contains the depth of footing, representing the fact that the volume of soil that resists a load increases with depth. Interestingly, the increase of bearing capacity over depth is more significant for LPDs than for mare and highland areas, although reasons for this observation are unknown. The bearing capacity envelope of the three investigated regions down to a depth of ~ 5 m might support the design and construction of shallow foundations for future infrastructure elements used for long-term exploration (Sanders & Larson, 2013) or ISRU purposes such as habitats, radiation shields, storage units, or scientific instruments such as large telescopes. Figures 2, 3, and S9 also include measurements that appear to reflect a consolidated type of regolith at depth. We note that the thickness of the regolith has been shown to vary greatly from as little as 2 m in some regions to as much as 15 m in others (Bart et al., 2011; McKay et al., 1991). This variation in regolith thickness is important when interpreting bearing capacities derived from boulder track measurements at larger depths since large rockfalls can potentially penetrate below the unconsolidated regolith. The bearing capacity derived from deep penetrating boulder tracks would then reflect the bearing capacity of the deep, consolidated layers and thus would be much higher, as displayed in Figures 2, 3, S8, and S9 with bearing capacity values reaching up to ~ 800 kPa and beyond. Using the shallowest unconsolidated regolith thickness estimates, potential tracks that carved into consolidated material have been identified and marked (Table S5 and Figure S10).

To further illuminate the results derived here based on orbital observations of boulder tracks, we compare them with results derived from previous Apollo-era missions. First, using the identical equations, the bearing capacities derived from measurements of boulder tracks in photographs taken during the Apollo 17 mission are calculated (Figures 3b and 4). Second, bearing capacities for shallower depths based on measurements in photographs taken from Surveyor 3 footpads, Apollo 11 bootprints, Apollo 12 LM footpads, Apollo 14 MET tracks, and Apollo 15/16 LRV tracks are calculated (Figures 3b and 4). In addition, bearing capacity results from Lunokhod 1 tracks are included in the comparison (Figure 4). Bearing capacities derived with different measurement methods correlate well and provide a similar lower limit for bearing capacity in mare highland and LPD regions. As additional support, photographs of LRV tracks in the three investigated regions have been analyzed in a qualitative manner (Figure S13). The LRV tracks show no region-dependent differences, potentially supporting the assumption of a linear-type bearing capacity envelope as described by equations (11) and (12). Here the regolith at *Shorty Crater*, Apollo 17 station 4, is assumed to approximate LPD regolith. However, the surface material next to station 4 might not be entirely representative for the regolith encountered in large-scale pyroclastic deposits.

Bearing capacities calculated based on boulder tracks measured in Apollo ground imagery tend to fall on the lower side of the point cloud in Figure 3b, while staying within the results derived using NAC imagery. Potential explanations of this tendency could be that the regolith in the Apollo 17 area actually has a slightly lower bearing capacity or that there is a slight bias in the observations and measurements of track properties in the Apollo imagery. For example, a bias could be introduced by the different viewing geometry or spatial resolution of the Apollo-era images.

The extrapolated bearing capacity envelope (Figure 3b) has been used to assess the trafficability of LPDs, mare, and highland regions, using the relation between vehicle mass and effective contact area between vehicle and soil (equation (10)). To do so, current rover design specifications for LER, Resource Prospector, Yutu, SpaceBok-, Spot-, and RHex-type rovers have been modified to explore the parameter space and simulate potential surcharge load due to additional crew or collected specimens during a science or resource extraction mission (Figure 5). Results indicate that Yutu's sinkage is limited within the applied parameter space, with sinkage only significantly increasing with narrow wheels. A modification of wheel width appears to be an effective way to ensure that a rover, in particular the LER, is capable of traversing

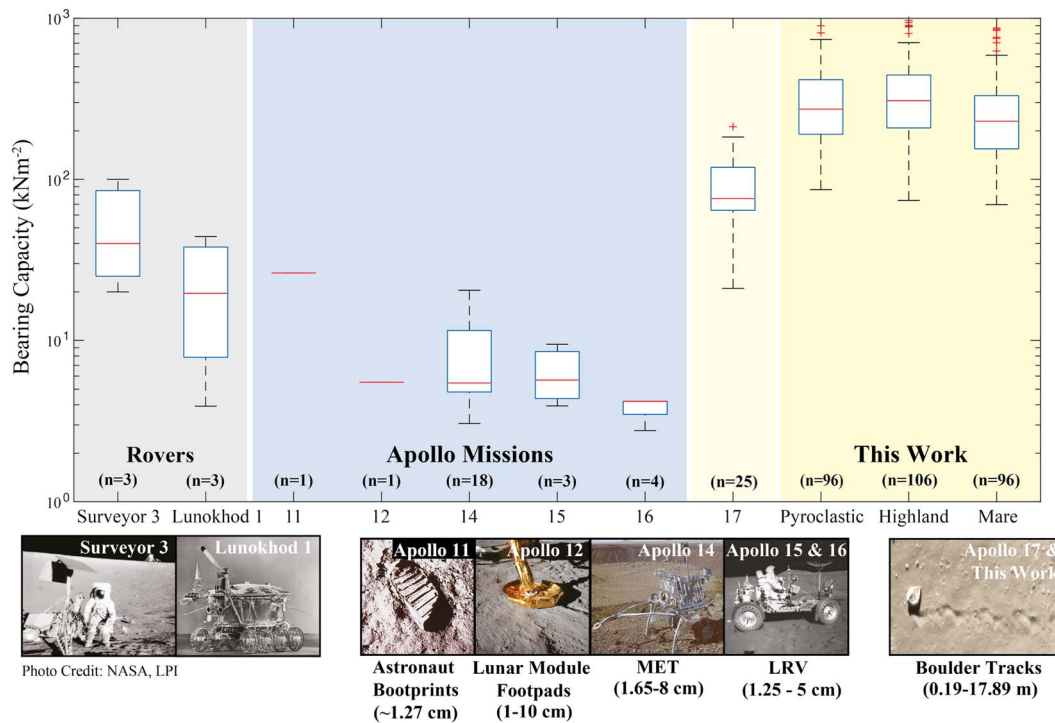


Figure 4. Comparison of bearing capacity values in this work and those calculated from literature values, including from different vehicles and objects, that is, astronaut bootprints, rover wheels, lander footpads, and rockfalls (Jaffe, 1971). Values used in calculations are taken from Apollo preliminary science reports 11–17 (Mitchell, Bromwell, et al., 1972; Mitchell et al., 1973; Mitchell, Carrier, et al., 1972). Lunokhod 1 bearing capacity values have not been calculated with the method presented in this paper but have been transferred from kg/cm^2 to kN/m^2 (Basilevsky et al., 2015). Bearing capacity values are dependent on depth; that is, small bearing capacity values reflect shallow penetration depths of the respective vehicle (e.g., landing pads). Black lines in box plots indicate the median of the respective data set, and red crosses indicate outliers. Highland and mare data are taken from widespread locations, and the average regolith thicknesses within those materials, from the literature, are used to constrain estimated regolith thickness. This explains overlap in sample numbers.

LPDs and other lunar regions. Figure 5 also illustrates that legged walking and jumping rovers like Spot- and SpaceBok-type robots, as well as hybrids like RHex, are able to traverse LPDs, using the extrapolated bearing capacity envelope. Like for wheeled rovers, sinkage of legged robots could be effectively limited by adapting the footpad width. For wheeled rovers, extra mass due to collected samples, as well as wheel diameter appear to have smaller influence on the estimated sinkage. In contrast to wheeled rovers, the investigated legged robots appear to be more susceptible to sinkage as a function of increasing weight. These deliberations do not consider detailed effects of modified wheel diameter-width ratio or footpad size on other trafficability aspects such as propulsion and energy consumption, however.

The assessment of LPD trafficability has implications for the design of future missions. A high-priority target for robotic and crewed missions is the pyroclastic vent in the Schrödinger basin, but it has been unclear whether wheeled or legged assets are able to traverse its periphery and to access its center (Allender et al., 2019; Bunte et al., 2011; O'Sullivan et al., 2011; Potts et al., 2015; Steenstra et al., 2016). The results of this study provide no evidence that the previous assumption of a traversable surface around the vent is invalid, thus, surface missions in this and similar locations may be possible using existing and proposed rover designs. Besides optimizing wheel or footpad width to avoid sinkage, a safe alternative could be to adapt the diameter of the wheels. Because bearing capacity values appear to be remarkably high at depths larger than 0.19 m, wheels with diameters >38 cm should not encounter flotation issues, based on the results of this study. However, such an increase in wheel diameter would require sufficient rover ground clearance and could result in an increased rolling resistance—among others—and, thus, would demand motors that can produce higher torque—depending on the effective sinkage.

Based on the results of this study, the interior of Schrödinger basin's vent may be traversable as well, concerning near surface bearing capacity. The bearing capacity envelope developed here as a function of

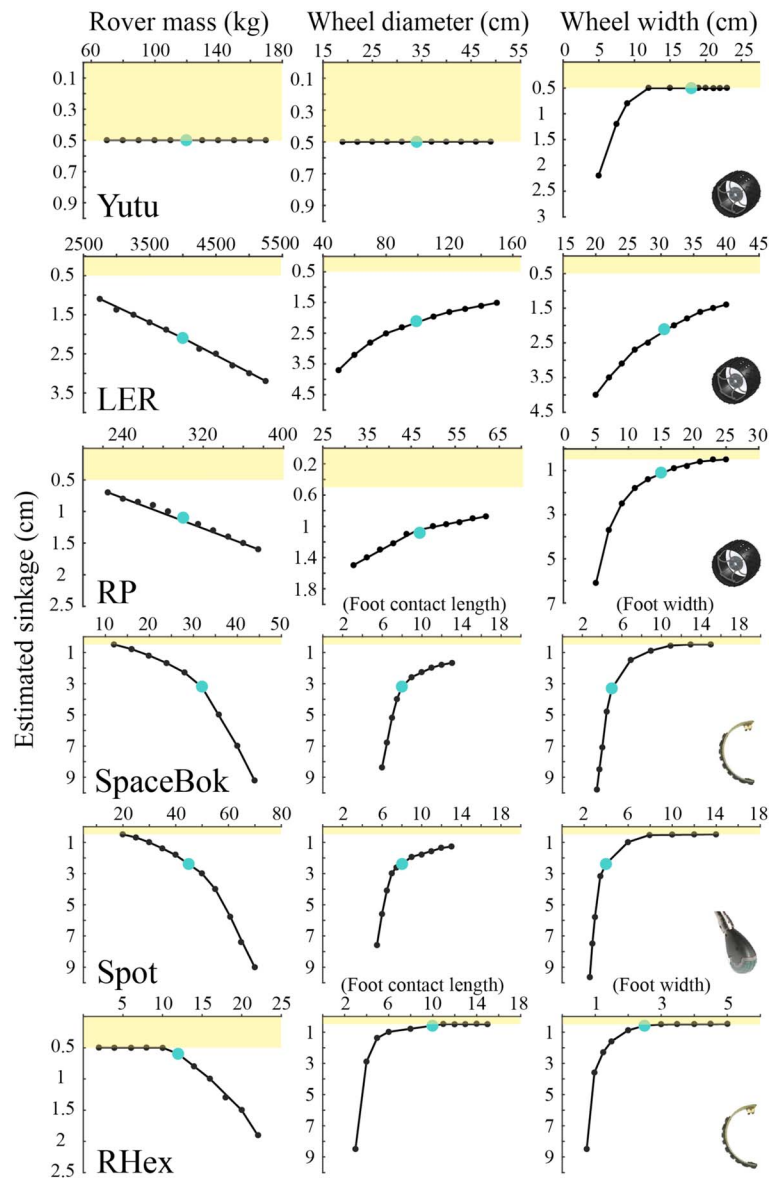


Figure 5. Yutu, LER, RP, SpaceBok-, Spot-, RHex-type rover estimated sinkage as function of difference in mass, wheel diameter/foot contact length, and wheel/foot width, based on derived bearing capacity values. All wheels/legs touch the ground. Cyan point denotes the sinkage using the default vehicle design specifications. Shaded area marks depth range from 0 to 0.5 cm, where sinkage has not been calculated. Vehicle specifications have been taken or inferred from Carrier et al. (1991), Asnani et al. (2009), ESA EO, n.d.-a/ESA EO, n.d.-b), W. J. Bluethmann (personal communication, 2018), NASA SEV (2010), Boston Dynamics (2019), SpaceBok (2017), and photographs/blueprints (where information was not directly accessible). Vehicle details are available in Table S2. SEV = Space Exploration Vehicle; RP = Resource Prospector; LER = Lunar Electric Rover.

slope angle could be used to produce a map of the vent and its surrounding that illustrates the spatial distribution of bearing capacity and identifies no-go areas for specific vehicles, similar to a maximum-traversable slope angle map used for mission planning. Further, the findings of this work could support the assessment and adjustment of vehicle properties in order to optimize the locomotion performance of rovers like the LER within and outside of the vent. Thus, the results of this study help to reduce and better anticipate risk related to future exploration and ISRU missions to the pyroclastic vent in the Schrödinger basin as well as similar sites on the Moon. It has to be noted that this study investigated LPD trafficability in terms of bearing capacity (wheel sinkage) only. In steep terrain, such as pyroclastic vents, other trafficability parameters become important for a successful traverse, for example, wheel slip and traction.

Acknowledgments

The authors would like to acknowledge the support of the Lunar and Planetary Institute (LPI) in Houston, TX, and the Universities Space Research Association. Funding was provided by the NASA Solar System Exploration Research Virtual Institute (NNXA14AB07A, PI David A. Kring). The research was performed as part of the Exploration Science Summer Intern Program hosted by the LPI and the NASA Johnson Space Center in Houston, TX. The authors thank William J. Bluethmann of NASA's Human Robotic Systems Project and Julie D. Stopar of the LPI for their willingness to provide insights about the LER and LROC systems, respectively. In addition, the authors would like to acknowledge the ideas of Christian Venturino presented during a previous LPI Exploration Science Summer Internship boulder track-related project. Moreover, one of us (V. T. B.) gratefully acknowledges financial support from the International Max Planck Research School at the Max Planck Institute for Solar System Research (IMPRS) and the Engineering Geology Group, Department of Earth Sciences, Swiss Federal Institute of Technology Zurich (ETHZ). This research has made use of the USGS Integrated Software for Imagers and Spectrometers (ISIS) and the Ames Stereo Pipeline (ASP). Due to online storage limitations, data can only be made available upon request to the authors. Alternatively, used data can be retrieved from the cited references or from the LROC image archive: <http://wms.lroc.asu.edu/lroc/search>. All used NAC image IDs can be found in the supporting information (Table S8). This is LPI contribution 2166. The study was conceived by D. A. K and implemented by V. T. B., C. I. H., S. N. M., A. R., and H. M. S. with D. A. K. ISRU issues were addressed by C. I. H., A. R., and H. M. S., while V. T. B., C. I. H., S. N. M., A. R., and H. M. S. selected sites of interest. V. T. B. processed imagery and DEMs; V. T. B. and H. M. S. conceived the implementation of bearing capacity equations; S. N. M. and A. R. built the GIS and performed measurements; and V. T. B. performed the trafficability analysis. V. T. B., C. I. H., S. N. M., A. R., and H. M. S. analyzed the results and wrote the first draft of the paper. All authors contributed to a discussion of findings, their implications for future missions, and editing the paper. The authors thank Ralph Lorenz, an anonymous reviewer, and Associate Editor Elizabeth Turtle for their constructive comments.

6. Conclusions

This work uses measurements of boulder tracks in NAC imagery to derive the bearing capacity of LPD, mare, and highland regions to assess their trafficability. A statistical analysis of the results suggests that all investigated regions have similar bearing capacity values from 0.19 to a depth of ~5 m and along varying slope gradients, where bearing capacity increases with depth and decreases with higher local slope gradients. In addition, LPDs exhibit statistically equal or significantly higher bearing capacities than mare and highland regions in all investigated depth ranges. Results indicate that the influence of geomorphological context and genesis on bearing capacity is limited over the observed depth and slope range. Qualitative observations of boulder tracks in all regions of interest show no region-based differences and, thus, support the quantitative analysis.

Results derived with the implemented equations using remote measurements correlate well with results derived using data collected in photographs taken during the past Surveyor and Apollo missions, as well as in situ during the past Lunokhod lunar surface missions. The high degree of statistical correlation between mare and highland areas, as well as the in situ-based values, is used to establish a general bearing capacity distribution trend from the surface down to a depth of ~5 m. As LPDs generally display equal or significantly higher bearing capacity values based on the statistical analysis along the observable depth range, this general trend is anticipated to be representative for LPDs as well, assuming that mechanical strength of LPD regolith is only caused by the considered parameters. A comparison of LRV tracks in the three investigated regions potentially supports this hypothesis.

Based on this assumption, the derived general bearing capacity distribution enables an analysis of the estimated sinkage of current and potential future rover designs as a measure for surface trafficability. The analysis shows no evidence that LPDs are not able to generally bear even heavy vehicles such as the LER. Therefore, this study promotes the feasibility of previously proposed traverses into untraversed lunar regions, including high-priority targets such as the surrounding and potentially the center of the pyroclastic vent in Schrödinger basin (Allender et al., 2019; Bunte et al., 2011; O'Sullivan et al., 2011; Steenstra et al., 2016). In addition, this study investigates changes in rover specifications such as wheel/footpad width, pad contact length, and wheel diameter and simulates extra mass caused by sample collection and finds that vehicle sinkage could be effectively limited by an optimization of wheel and pad width. Wheel diameters larger than 38 cm could be an alternative to assure trafficability of vehicles in LPDs, to the potential cost of higher rolling resistance, requiring larger driving torque. For example, the radii of the wheels on the prototype LER (34.3 cm; Harrison et al., 2008) and on the anticipated flight version of it (49 cm, NASA SEV, 2010) exceed 19 cm. Thus, that vehicle should be able to traverse pyroclastic deposits. Other applications of this study's findings potentially include the design of foundations for exploration and ISRU infrastructure, as well as heavy instrumentation.

References

- Allen, C. C., Morris, R. V., & McKay, D. S. (1996). Oxygen extraction from lunar soils and pyroclastic glass. *Journal of Geophysical Research*, 101(E11), 26,085–26,095. <https://doi.org/10.1029/96JE02726>
- Allender, E. J., Orgel, C., Almeida, N. V., Cook, J., Ende, J. J., Kamps, O., et al. (2019). Traverses for the ISECG-GER design reference mission for humans on the lunar surface. *Advances in Space Research*, 63(1), 692–727. <https://doi.org/10.1016/j.asr.2018.08.032>
- Asnani, V., Delap, D., & Creager, C. (2009). The development of wheels for the lunar roving vehicle. *Journal of Terramechanics*, 46(3), 89–103. <https://doi.org/10.1016/j.jterra.2009.02.005>
- Baedecker, P., Chou, C.-L., Sundberg, L., & Wasson, J. (1974). Volatile and siderophilic trace elements in the soils and rocks of Taurus-Littrow. Paper presented at the Lunar and Planetary Science Conference Proceedings.
- Bart, G. D., Nickerson, R. D., Lawder, M. T., & Melosh, H. (2011). Global survey of lunar regolith depths from LROC images. *Icarus*, 215(2), 485–490. <https://doi.org/10.1016/j.icarus.2011.07.017>
- Basilevsky, A. T., Abdrakhimov, A. M., Head, J. W., Pieters, C. M., Wu, Y., & Xiao, L. (2015). Geologic characteristics of the Luna 17/Lunokhod 1 and Chang'E-3/Yutu landing sites, northwest Mare Imbrium of the Moon. *Planetary and Space Science*, 117, 385–400. <https://doi.org/10.1016/j.pss.2015.08.006>
- Bekker, M. G. (1956). *Theory of land locomotion. The Mechanics of Vehicle Mobility*. Ann Arbor: University of Michigan Press.
- Bekker, M. G. (1960). *Off-the-road locomotion. Research and Development in Terramechanics*. Ann Arbor: University of Michigan Press.
- Boston Dynamics (2019). Robots. Changing your idea of what robots can do. URL: <https://www.bostondynamics.com/robots> (Status: 01/28/2019).
- Bowles, L. (1997). *Foundation analysis and design*. McGraw-Hill International Book Company.
- Bunte, M. K., Porter, S., & Robinson, M. S. (2011). A sortie mission to Schrödinger Basin as reconnaissance for future exploration. In *Special Paper of the Geological Society of America* (Vol. 483, pp. 533–546). (Special Paper of the Geological Society of America; Vol. 483). [https://doi.org/10.1130/2011.2483\(32\)](https://doi.org/10.1130/2011.2483(32))

- Carrier, W. III, Olhoeft, G. R., & Mendell, W. (1991). Physical properties of the lunar surface. In *In the Lunar Source Book*, Chapter 9 (pp. 475–594). Cambridge University Press.
- Castelli, F., & Lentini, V. (2012). Evaluation of the bearing capacity of footings on slopes. *International Journal of Physical Modelling in Geotechnics*, 12(3), 112–118. <https://doi.org/10.1680/ijpmg.11.00015>
- Cho, G.-C., Dodds, J., & Santamarina, J. C. (2007). Closure to “Particle shape effects on packing density, stiffness, and strength: Natural and crushed sands” by Gye-Chun Cho, Jake Dodds, and J. Carlos Santamarina. *Journal of Geotechnical and Geoenvironmental Engineering*, 133(11), 1474–1474. [https://doi.org/10.1061/\(ASCE\)1090-0241\(2007\)133:11\(1474\)](https://doi.org/10.1061/(ASCE)1090-0241(2007)133:11(1474))
- Chou, C. L., Boynton, W. V., Sundberg, L. L., & Wasson, J. T. (1975). Volatiles on the surface of Apollo 15 green glass and volatile-element systematics in soils from edges of mare basins. In *Lunar Science Conference, 6th* (Vol. 2, pp. 1701–1727). Houston, TX, New York: Pergamon Press
- Coduto, D. P., Yeung, M.-c. R., & Kitch, W. A. (2011). *Geotechnical engineering: Principles and practices*. London: Pearson.
- Costes, N., Carrier, W. III, Mitchell, J., & Scott, R. (1970). Apollo 11 soil mechanics investigation. *Science*, 167(3918), 739–741. <https://doi.org/10.1126/science.167.3918.739>
- Costes, N. C., Farmer, J. E., & George, E. B., (1972). Mobility performance of the lunar roving vehicle: Terrestrial studies – Apollo 15 Results. (December), p.87.
- Durgunoglu, H. T., & Mitchell, J. K. (1975). Static penetration resistance of soils: I - Analysis. In *Proc. Specialty Conf. on In Situ Measurement of Soil Properties* (pp. 151–171). Raleigh: American Society of Civil Engineers.
- Eggleston, J., Patterson, A., Throop, J., Arant, W., & Spooner, D. (1968). Lunar rolling stone. *Photogrammetric Engineering*, 34, 246–255.
- ESA EO. (n.d.-a). Chang’e-3 Moon-landing mission. URL: <https://earth.esa.int/web/eoportal/satellite-missions/c-missions/chang-e-3> (Status: 08/14/2018).
- ESA EO. (n.d.-b). Chang’e-4 far side Moon-landing mission of China. URL: <https://directory.eoportal.org/web/eoportal/satellite-missions/c-missions/chang-e-4> (Status: 10/01/2018).
- Eugster, O., Eberhardt, P., Geiss, J., Grögler, N., Jungck, M., & Mörgeli, M. (1977). The cosmic-ray exposure history of Shorty Crater samples: The age of Shorty crater. In *Proc. 8th Lunar Planet. Sci. Conf.* (pp. 3059–3082). New York: Pergamon Press, Inc.
- Eurocode7 (1996). Eurocode 7: Geotechnical design. BS EN 1997–1:2004, EN 1997–1:2004.
- Filice, A. L. (1967). Lunar surface strength estimate from Orbiter II photograph. *Science*, 156(3781), 1486–1487. <https://doi.org/10.1126/science.156.3781.1486>
- Florensky, C. P., Basilevsky, A. T., Bobina, N. N., Burba, G. A., Grebennik, N. N., Kuzmin, R. O., et al. (1978). The floor of crater Le Monier: A study of Lunokhod 2 data. In *Proc. Lunar Planet. Sci. Conf.* (Vol. 1978, pp. 1449–1458). New York: Pergamon Press, Inc.
- Gaddis, L. R., Staid, M. I., Tyburczy, J. A., Hawke, B. R., & Petro, N. E. (2003). Compositional analyses of lunar pyroclastic deposits. *Icarus*, 161(2), 262–280. [https://doi.org/10.1016/S0019-1035\(02\)00036-2](https://doi.org/10.1016/S0019-1035(02)00036-2)
- Hansen, J. B. (1970). A revised and extended formula for bearing capacity. Bulletin No. 11, The Danish Geotechnical Institute.
- Harrison, D. A., Ambrose, R., Bluethmann, B., & Junkin, L. (2008). Next generation rover for lunar exploration. JSC released document, IEEEAC paper #1196, 13 pages.
- Houston, W. N., Hovland, H. J., Mitchell, J. K., & Namiq, L. I. (1972). Lunar soil porosity and its variation as estimated from footprints and boulder tracks. *Proc. Of the 3rd Lunar Sci. Conf. (Supp. 3, Geochimica et Cosmochimica Acta)*, 3, 3255–3263.
- Hovland, H., & Mitchell, J. (1969). Friction angle of lunar surface soils estimated from boulder tracks: Space sciences laboratory. Lunar Surface Engineering Properties Experiment Definition, Second Quarterly Report, Univ. of California.
- Hovland, H. J., & Mitchell, J. K. (1971). Lunar surface engineering properties experiment definition. Volume 2: Mechanics of rolling sphere-soil slope interaction. Final report.
- Hovland, H. J., & Mitchell, J. K. (1973). Boulder tracks and nature of lunar soil. *The Moon*, 6(1–2), 164–175. <https://doi.org/10.1007/BF02630660>
- IEEE Spectrum (2010). Forgotten Soviet Rover beams light back to Earth. URL: <https://spectrum.ieee.org/tech-history/space-age/forgotten-soviet-moon-rover-beams-light-back-to-earth> (Status: 08/14/2018).
- ISRO. (n.d.). GSV-F10/Chandrayaan-2 mission. URL: <https://www.isro.gov.in/gslv-f10-chandrayaan-2-mission> (Status: 10/01/2018).
- Jaffe, L. D. (1971). Bearing strength of lunar soil. *The moon*, 3(3), 337–345. <https://doi.org/10.1007/BF00561845>
- Kring, D. A., Durda, D. D. (2012). A global lunar landing site study to provide the scientific context for exploration of the Moon. Lunar and Planetary Institute. Contribution #1694, pp. 688.
- Kring, D. A., Kramer, G. Y., Bussey, D. B. J., & Hurley, D. M. (2014). Prominent volcanic source of volatiles in the south polar region of the Moon. Annual Meeting of the Lunar Exploration Analysis Group, Laurel, Maryland. LPI Contribution No. 1820, #3057.
- Kusakabe, O., Kimura, T., & Yamaguchi, H. (1981). Bearing capacity of slopes under strip loads on the top surfaces. *Soils and Foundations*, 21(4), 29–40. https://doi.org/10.3208/sandf1972.21.4_29
- LExSWG. (1995). Lunar surface exploration strategy. Lunar Exploration Science Working Group, Final Advisory Group Report. URL: <https://www.lpi.usra.edu/lunar/strategies/LExSWG.pdf> (Status: 08/16/2018).
- LPI USRA. (n.d.). The Lunar Orbiter Program. URL: <https://www.lpi.usra.edu/lunar/missions/orbiter/>. (Status: 08/14/2018).
- McKay, D. S., Heiken, G., Basu, A., Blanford, G., Simon, S., Reedy, R., et al. (1991). The lunar regolith. In *The Lunar Source Book* (Chap. 7, pp. 285–356). Cambridge University Press.
- Melosh, H. J. (2011). *Planetary Surface Processes*. Cambridge University Press.
- Meyerhof, G. (1951). The ultimate bearing capacity of foundations. *Geotechnique*, 2(4), 301–332. <https://doi.org/10.1680/geot.1951.2.4.301>
- Meyerhof, G. (1957). The ultimate bearing capacity of foundations on slopes. Paper presented at the Proc., 4th Int. Conf. on Soil Mechanics and Foundation Engineering.
- Mitchell, J., Bromwell, L., Carrier III, W., Costes, N., Houston, W., & Scott, R. (1972). Soil mechanics experiments. In Apollo 15 Preliminary Science Report, NASA SP-289, Section 7, 1–28.
- Mitchell, J., Houston, W., Carrier III, W., & Costes, N. (1974). Apollo soil mechanics experiment, S-200, Final Report, Space Sciences Laboratory Series 15, Issue 7.
- Mitchell, J., Houston, W., Scott, R., Costes, N., Carrier III, W., & Bromwell, L. (1972). Mechanical properties of lunar soil: Density, porosity, cohesion and angle of internal friction. Paper presented at the Lunar and Planetary Science Conference Proceedings.
- Mitchell, J. K., Carrier III, W. D., Costes, N. C., Houston, W. N., Scott, R. F., & Hovland, H. J. (1973). Soil mechanics. In Apollo 17 Preliminary Science Report, NASA SP-300, Section 8, 1–22.
- Mitchell, J. K., Carrier III, W. D., Houston, W. N., Scott, R. F., Bromwell, L. G., Durgunoglu, H., Costes, N. C. (1972). Soil mechanics. In Apollo 16 Preliminary Science Report, pp. 8–1 8–29. NASA SP-315.

- Moore, H. J. (1970). Estimates of the mechanical properties of lunar surface using tracks and secondary impact craters produced by blocks and boulders. NASA Interagency Report: Astrogeology 22.
- Moore, H. J., Vischer, W. A., & Martin, G. L. (1972). Boulder tracks on the Moon and Earth. U.S. Geol. Survey Prof. Paper 800-B, 1972, pp. B165-B174.
- Muehlberger, W. R., Batson, R. M., Cernan, E. A., Freeman, V. L., Hait, M. H., Holt, H. E., et al. (1973). Preliminary geologic investigation of the Apollo 17 landing site. In Apollo 17 Preliminary Science Report, NASA SP-330, Section 6, 1–91.
- NASA Apollo 11 (2017). Apollo 11 Mission Overview. URL: https://www.nasa.gov/mission_pages/apollo/missions/apollo11.html (Status: 08/14/2018).
- NASA SEV (2010). Space Exploration Vehicle Concept, NASA facts. URL: https://www.nasa.gov/pdf/464826main_SEV_Concept_FactSheet.pdf (Status: 08/28/2018).
- National Research Council (NRC) (2007). *The scientific context for exploration of the Moon*. Washington, DC: National Academies Press.
- National Space Science Data Center (2006). Surveyor, 1966–1968. URL: <https://nssdc.gsfc.nasa.gov/planetary/lunar/surveyor.html>. (Status: 08/14/2018).
- National Space Science Data Center (2016). The Apollo lunar roving vehicle. URL: https://nssdc.gsfc.nasa.gov/planetary/lunar/apollo_lrv.html (Status: 08/14/2018).
- National Space Science Data Center (2017). Luna21/Lunokhod 2. URL: <https://nssdc.gsfc.nasa.gov/nmc/spacecraftDisplay.do?id=1973-001A> (Status: 08/14/2018).
- O'Sullivan, K. M., Kohout, T., Thaisen, K. G., & Kring, D. A. (2011). Calibrating several key lunar stratigraphic units representing 4 billion years of lunar history within Schrödinger basin. In D. A. Williams, & W. Ambrose (Eds.), *Recent Advances in Lunar Stratigraphy* (pp. 117–128). Boulder, CO: Geological Society of America Special Paper 477.
- Pike, R. J. (1971). Some preliminary interpretations of lunar mass-wasting process from Apollo 10 photography. In *Analysis of Apollo 10 Photography and Visual Observations*. NASA SP-232 (pp. 14–20). Washington, DC: NASA.
- Potts, N. J., Gullikson, A. L., Curran, N. M., Dhaliwal, J. K., Leader, M. K., Rege, R. N., et al. (2015). Robotic traverse and sample return strategies for a lunar farside mission to the Schrödinger basin. *Advances in Space Research*, 55(4), 1241–1254. <https://doi.org/10.1016/j.asr.2014.11.028>
- Sanders, G. B., & Larson, W. E. (2013). Progress Made in Lunar In Situ Resource Utilization under NASA's Exploration Technology and Development Program. *Journal of Aerospace Engineering*, 26(1). [https://doi.org/10.1061/\(ASCE\)AS.1943-5525.0000208](https://doi.org/10.1061/(ASCE)AS.1943-5525.0000208)
- Saran, S., Sud, V., & Handa, S. (1989). Bearing capacity of footings adjacent to slopes. *Journal of Geotechnical Engineering*, 115(4), 553–573. [https://doi.org/10.1061/\(ASCE\)0733-9410\(1989\)115:4\(553\)](https://doi.org/10.1061/(ASCE)0733-9410(1989)115:4(553))
- Scholten, F., Oberst, J., Matz, K. D., Roatsch, T., Wählisch, M., Speyerer, E., & Robinson, M. (2012). GLD100: The near-global lunar 100 m raster DTM from LROC WAC stereo image data. *Journal of Geophysical Research*, 117, E00H17. <https://doi.org/10.1029/2011JE003926>
- Scott, R., Carrier, W. III, Costes, N., & Mitchell, J. (1971). Apollo 12 soil mechanics investigation. *Geotechnique*, 21(1), 1–14. <https://doi.org/10.1680/geot.1971.21.1.1>
- Shean, D. E., Alexandrov, O., Moratto, Z. M., Smith, B. E., Joughin, I. R., Porter, C., & Morin, P. (2016). An automated, open-source pipeline for mass production of digital elevation models (DEMs) from very-high-resolution commercial stereo satellite imagery. *ISPRS Journal of Photogrammetry and Remote Sensing*, 116, 101–117. <https://doi.org/10.1016/j.isprsjprs.2016.03.012>
- Shill, S., & Hoque, M. (2015). Comparison of bearing capacity calculation methods in designing shallow foundations. Gazipur, Bangladesh.
- Slyuta, E. (2014). Physical and mechanical properties of the lunar soil (a review). *Solar System Research*, 48(5), 330–353. <https://doi.org/10.1134/S0038094614050050>
- SpaceBok (2017). The SpaceBok project. URL: <http://spacebok.ch/> (Status: 01/29/2019).
- Steenstra, E. S., Martin, D. J., McDonald, F. E., Paisarnsombat, S., Venturino, C., O'Hara, S., et al. (2016). Analyses of robotic traverses and sample sites in the Schrödinger basin for the HERACLES human-assisted sample return mission concept. *Advances in Space Research*, 58(6), 1050–1065. <https://doi.org/10.1016/j.asr.2016.05.041>
- Terzaghi, K. (1951). *Theoretical soil mechanics*. London: Chapman And Hall, Limited.
- Vesic, A. S. (1973). Analysis of ultimate loads of shallow foundations. *Journal of Soil Mechanics & Foundations Div*, 99(sm1), 45–73.
- Wasson, J. T., Boynton, W. V., Kallemeyn, G. W., Sundberg, L. L., & Wai, C. M. (1976). Volatile compounds released during lunar lava fountaining. In *Lunar Science Conference, 7th, Houston, Tex., Proceedings* (Vol. 2, pp. 1583–1595). New York: Pergamon Press, Inc.

References From the Supporting Information

- CGSociety (2014). Next Generation Lunar Electric Rover by NASA, by Alexscape (3D). URL: <http://forums.cgsociety.org/t/next-generation-lunar-electric-rover-by-nasa-by-alexscape-alexscape-3d/1660613> (Status: 01/30/2019).
- Fa, W., & Jin, Y. (2010). A primary analysis of microwave brightness temperature of lunar surface from Chang-E 1 multi-channel radiometer observation and inversion of regolith layer thickness. *Icarus*, 207(2), 605–615. <https://doi.org/10.1016/j.icarus.2009.11.034>
- Giguere, T. A., Taylor, G. J., Hapke, B. R., & Lucey, P. G. (2010). The titanium contents of lunar mare basalts. *Meteoritics and Planetary Science*, 35(1), 193–200.
- Lucey, P. G. (2004). Mineral maps of the Moon. *Geophysical Research Letters*, 31, L08701. <https://doi.org/10.1029/2003GL019406>
- Lucey, P. G., Blewett, D. T., & Jolliff, B. L. (2000). Lunar iron and titanium abundance algorithms based on final processing of Clementine ultraviolet-visible images. *Journal of Geophysical Research*, 105(E8), 20,297–20,305. <https://doi.org/10.1029/1999JE001117>
- Oberbeck, V. R., & Quaide, W. L. (1968). Genetic implications of lunar regolith thickness variations. *Icarus*, 9(1-3), 446–465. [https://doi.org/10.1016/0019-1035\(68\)90039-0](https://doi.org/10.1016/0019-1035(68)90039-0)
- Olhoeft, G. R., & Strangway, D. W. (1975). Dielectric properties of the first 100 meters of the Moon. *Earth and Planetary Science Letters*, 24(3), 394–404. [https://doi.org/10.1016/0012-821X\(75\)90146-6](https://doi.org/10.1016/0012-821X(75)90146-6)
- Osp.mans.edu.eg. (n.d.). Bearing capacity and stability of foundations. URL: <http://osp.mans.edu.eg/sfoundation/bearing.htm> (Status: 01/28/2019).
- Room Space Journal (n.d.). Resource prospector—A lunar pathfinder. URL: <https://room.eu.com/article/resource-prospector-a-lunar-pathfinder> (Status: 01/30/2019).
- Sato, H., Robinson, M. S., Lawrence, S. J., Denevi, B. W., Hapke, B., Jolliff, B. L., & Hiesinger, H. (2017). Lunar mare TiO₂ abundances estimated from UV/Vis reflectance. *Icarus*, 296, 216–238. <https://doi.org/10.1016/j.icarus.2017.06.013>

- Shuratov, Y. G., & Bondarenko, N. V. (2001). Regolith layer thickness mapping of the Moon by radar and optical data. *Icarus*, *149*(2), 329–338. <https://doi.org/10.1006/icar.2000.6545>
- Strangway, D., Pearce, G., & Olhoeft, G. (1975). Magnetic and dielectric properties of lunar samples. In A. P. Vinogradov (Ed.), *Kosmochimiya Luny i Planet*, (pp. 712–728). Moscow: Nauka. [In Russian]
- Thingiverse (2014). Mars Curiosity Rover wheel assembly, 3D Model. URL: <https://www.thingiverse.com/thing:229631> (Status: 01/30/2019).